AOS THESIS

Optimized Artificial Intelligence for Enhanced Ectasia Detection Using Scheimpflug-Based Corneal Tomography and Biomechanical Data

RENATO AMBRÓSIO JR, AYDANO P. MACHADO, EDILEUZA LEÃO, JOÃO MARCELO G. LYRA, MARCELLA Q. SALOMÃO, LOUISE G. PELLEGRINO ESPORCATTE, JOÃO B.R. DA FONSECA FILHO, ERICA FERREIRA-MENESES, NELSON B. SENA JR, JORGE S. HADDAD, ALEXANDRE COSTA NETO, GILDASIO CASTELO DE ALMEIDA JR, CYNTHIA J. ROBERTS, AHMED ELSHEIKH, RICCARDO VINCIGUERRA, PAOLO VINCIGUERRA, JENS BÜHREN, THOMAS KOHNEN, GUY M. KEZIRIAN, FARHAD HAFEZI, NIKKI L. HAFEZI, EMILIO A. TORRES-NETTO, NANJI LU, DAVID SUNG YONG KANG, OMID KERMANI, SHIZUKA KOH, PREMA PADMANABHAN, SUPHI TANERI, WILLIAM TRATTLER, LUCA GUALDI, JOSÉ SALGADO-BORGES, FERNANDO FARIA-CORREIA, ELIAS FLOCKERZI, BERTHOLD SEITZ, VISHAL JHANJI, TOMMY C.Y. CHAN, PEDRO MANUEL BAPTISTA, DAN Z. REINSTEIN, TIMOTHY J. ARCHER, KAROLINNE M. ROCHA, GEORGE O. WARING IV, RONALD R. KRUEGER, WILLIAM J. DUPPS, RAMIN KHORAMNIA, HASSAN HASHEMI, SOHEILA ASGARI, HAMED MOMENI-MOGHADDAM, SIAMAK ZAREI-GHANAVATI, ROHIT SHETTY, POOJA KHAMAR, MICHAEL W. BELIN, AND BERNARDO T. LOPES

- PURPOSE: **To optimize artificial intelligence (AI) algorithms to integrate Scheimpflug-based corneal tomography and biomechanics to enhance ectasia detection.**
- DESIGN: **Multicenter cross-sectional case-control retrospective study.**
- METHODS: **A total of 3886 unoperated eyes from 3412 patients had Pentacam and Corvis ST (Oculus**

Author Bio available at AJO.com.

Meeting Presentation: This work was partially presented as a paper in the virtual meeting of the ASCRS (American Society of Cataract and Refractive Surgery) 2020.

Accepted for publication December 12, 2022.

From the Department of Ophthalmology, the Federal University of the State of Rio de Janeiro, Brazil; Rio de Janeiro Corneal Tomography and Biomechanics Study Group, Rio de Janeiro, Brazil; Department of Ophthalmology, Federal University of São Paulo, São Paulo, Brazil; Brazilian Artificial Intelligence Networking in Medicine (BrAIN), Maceio and Rio de Janeiro, Brazil; World College of Refractive Surgery & Visual Sciences, Scottsdale, Arizona, USA; Computing Institute, Federal University of Alagoas, Brazil; Universidade Estadual de Ciências da Saúde de Alagoas (UNCISAL), Maceio, Alagoas, Brazil; Department of Ophthalmology & Visual Sciences, Department of Biomedical Engineering, the Ohio State University, Columbus, Ohio, USA; The School of Engineering, University of Liverpool, Liverpool, United Kingdom; Beijing Advanced Innovation Center for Biomedical Engineering, Beihang University, Beijing, China; NIHR Biomedical Research Centre for Ophthalmology, Moorfields Eye Hospital NHS Foundation Trust and UCL Institute of Ophthalmology, London, United Kingdom; Humanitas San Pio X Hospital, Milano, Italy; Department of Biomedical Sciences, Humanitas University, Milan, Italy; Humanitas Clinical and Research Center—IRCCS, Rozzano, Italy; Praxis für Augenheilkunde Prof. Bühren, Germany; Department of Ophthalmology, Goethe University Frankfurt, Frankfurt am Main, Germany; SurgiVision® Consultants, Inc, Scottsdale, Arizona, USA; ELZA Institute, Dietikon, Swisstzerland; Center for Applied Biotechnology and Molecular Medicine, University of Zurich, Zurich, Switzerland; USC Roski Eye Institute, Miller School of Medicine; Los Angeles, California, USA; School of Ophthalmology and Optometry, Wenzhou Medical University, Wenzhou, China; Faculty of Medicine and Health Sciences, University of Antwerp, Wilrijk, Belgium; Department of Ophthalmology, Antwerp University Hospital, Edegem, Belgium; Emmetropia Mediterranean Eye Institute, Heraklion, Greece; Eyereum Eye Clinic, Seoul, South Korea; Augenklinik am Neumarkt, Cologne, Germany; Department of Ophthalmology, Osaka University Graduate School of Medicine, Osaka, Japan; Department of Cornea and Refractive Surgery, Medical Research Foundation, Sankara Nethralaya, Chennai, Tamil Nadu, India; Center for Refractive Surgery Muenster, Muenster; University Eye-Clinic, Ruhr-University, Bochum, Germany; Center for Excellence in Eye Care, Miami, Florida, USA; Diagnostica Oftalmologica e Microchirurgia Oculare (DOMA), Rome, Italy; Clinica J. Salgado-Borges, Porto; Department of Ophthalmology, Hospital de Braga; Life and Health Sciences Research Institute (ICVS), Escola de Medicina, Universidade do Minho, Braga, Portugal; Department of Ophthalmology, Saarland University Medical Center, Homburg, Germany; Department of Ophthalmology and Visual Sciences, the Chinese University of Hong Kong, Hong Kong SAR, China; Department of Ophthalmology, University of Pittsburgh School of Medicine, Pittsburgh, PA, USA; Ophthalmology Department, Centro Hospitalar Universitário do Porto, Porto, Portugal; Reinstein Vision, London Vision Clinic, London, United Kingdom; Columbia University Medical Center, New York, New York, USA; Sorbonne Université, Paris, France; Biomedical Science Research Institute, Ulster University, Coleraine, United Kingdom; Storm Eye Institute, Medical University of South Carolina, Charleston; Waring Vision Institute, Mount Pleasant; South Carolina, Stanley M. Truhlsen Eye Institute, Department of Ophthalmology and Visual Sciences, University of Nebraska Medical Center, Omaha, Nebraska; Cole Eye Institute, Cleveland Clinic; Department of Biomedical Engineering, Lerner Research Institute; Department of Biomedical Engineering, Case Western Reserve University, Cleveland, Ohio, USA; The David J. Apple International Laboratory for Ocular Pathology, Department of Ophthalmology, University of Heidelberg, Heidelberg, Germany; Noor Ophthalmology Research Center, Noor Eye Hospital, Tehran, Iran; Rehabilitation Sciences Research Center, Zahedan University of Medical Sciences, Zahedan, Iran; Eye Research Center, Mashhad University of Medical Sciences, Mashhad, Iran; Department of Cornea and Refractive Surgery, Narayana Nethralaya, Bangalore, India; Department of Ophthalmology & Vision Science, University of Arizona, Tucson, Arizona, USA; Light for Sight Foundation, Dietikon; Instituto de Computação, Federal University of Alagoas, Maceio, Brazil.

Inquiries to Renato Ambrósio Jr, Department of Ophthalmology, the Federal University of the State of Rio de Janeiro, Rio de Janeiro, Brazil; e-mail: dr.renatoambrosio@gmail.com

0002-9394/$36.00
https://doi.org/10.1016/j.ajo.2022.12.016

Optikgeräte GmbH) examinations. The database included 1 eye randomly selected from 1680 normal patients (N) and from 1181 "bilateral" keratoconus (KC) patients, along with 551 normal topography eyes from patients with very asymmetric ectasia (VAE-NT), and their 474 unoperated ectatic (VAE-E) eyes. The current TBIv1 (tomographic-biomechanical index) was tested, and an optimized AI algorithm was developed for augmenting accuracy.

- **RESULTS:** **The area under the receiver operating characteristic curve (AUC) of the TBIv1 for discriminating clinical ectasia (KC and VAE-E) was 0.999 (98.5% sensitivity; 98.6% specificity [cutoff: 0.5]), and for VAE-NT, 0.899 (76% sensitivity; 89.1% specificity [cutoff: 0.29]). A novel random forest algorithm (TBIv2), developed with 18 features in 156 trees using 10-fold cross-validation, had a significantly higher AUC (0.945; DeLong, *P* < .0001) for detecting VAE-NT (84.4% sensitivity and 90.1% specificity; cutoff: 0.43; DeLong, *P* < .0001) and a similar AUC for clinical ectasia (0.999; DeLong, *P* = .818; 98.7% sensitivity; 99.2% specificity [cutoff: 0.8]). Considering all cases, the TBIv2 had a higher AUC (0.985) than TBIv1 (0.974; DeLong, *P* < .0001).**
- **CONCLUSIONS:** **AI optimization to integrate Scheimpflug-based corneal tomography and biomechanical assessments augments accuracy for ectasia detection, characterizing ectasia susceptibility in the diverse VAE-NT group. Some patients with VAE may have true unilateral ectasia. Machine learning considering additional data, including epithelial thickness or other parameters from multimodal refractive imaging, will continuously enhance accuracy. NOTE: Publication of this article is sponsored by the American Ophthalmological Society.** **(Am J Ophthalmol 2023;251: 126–142.**

REFRACTIVE SURGERY HAS STIMULATED TREMENDOUS advances in corneal imaging to enhance safety and predictability of elective and therapeutic procedures. As predicted by Wilson and Klyce[1] in 1991, advances in corneal analysis enable the surgeon to customize refractive corrections and enhance the efficacy to a level that Helmholtz, Placido, and Gullstrand would undoubtedly have been impressed. Nevertheless, the overwhelming data generated determined the need for more efficient ways to analyze the data. Artificial intelligence (AI), introduced in 1956, has gained increased relevance in ophthalmology with multiple potential applications.[2-6] AI algorithms use computer processing power to simulate and augment human interpretation. Such an approach enhances data analysis and the efficiency of clinical decisions by employing a consistent multidimensional assessment of the large volume of information available, such as when assessing data from multimodal corneal and refractive imaging.[7,8]

Maeda and associates[9] pioneered the field in describing a neural network (NN) model based on 11 Placido disk–based topography indices. The automated NN pattern interpretation provided a correct classification for all 108 maps in the training set but correctly classified only 80% (60 of 75) of the maps in the testing group. Although such a difference was statistically significant, the authors discussed the concept of reinforced learning for further refining the model and predicted the paradigm shift related to AI in the field.[9] Since then, AI has made a significant impact on the detection and treatment of keratoconus (KC) and ectatic corneal diseases (ECD).[10-24]

The paradigm shift in ECD management was related to introducing crosslinking and intrastromal corneal ring segments that could be used earlier in the disease process than penetrating keratoplasty.[25,26] These newer treatment modalities highlighted the importance of recognizing mild or subclinical ectatic disease, which is also paramount for identifying patients at risk for iatrogenic ectasia after corneal laser vision correction (LVC).[27] Assessing ectasia risk among elective refractive surgery candidates has evolved to the characterization of the inherent susceptibility of the cornea for biomechanical decompensation and ectasia progression, which lies beyond detecting mild cases with ECD.[28-30] In addition, the ectasia risk assessment should also include the impact of the LVC procedure, which has been heightened by studies involving finite element analysis.[31,32] This concept is in agreement with McGhee's 2-hit hypothesis that genetic (intrinsic) and environmental (extrinsic) factors play a role in the etiology of KC,[25] and the biomechanical cycle of decompensation of corneal ectasia proposed by Dupps and Roberts.[33]

Patients presenting with clinical ectasia in one eye but with the contralateral eye with normal anterior curvature (topography) and normal vision have been classically referred to as one of the possible categories of forme fruste KC (FFKC).[34] Although there are no unified criteria to define subclinical KC (SCKC) and FFKC in the literature,[35] such asymmetric cases have been studied using advanced imaging, such as corneal tomography, to demonstrate an improved ability to detect ECD at an early preclinical stage.[7,12,13,17,19,36-39] Such cases are referred to as very asymmetric ectasia (VAE)[17] or highly asymmetric ectasia.[19] In a study involving cases from Rio de Janeiro (Brazil) and Milan (Italy), the tomographic and biomechanical index (TBI) was developed with AI by applying random forest with leave-one-out cross-validation (RF/LOOCV). The training set included 94 normal topography eyes from patients with VAE (VAE-NT), along with 1 eye randomly selected from each of 480 normal patients, 1 eye randomly selected from 204 "bilateral" KC cases, and the 72 unoperated ectatic eyes (VAE-E). Considering the LOOCV result, the cutoff of 0.79 provided 100% sensitivity and specificity to detect clinical ectasia (KC + VAE-E cases).

An adjusted cutoff of 0.29 provided 96% specificity and 90.4% sensitivity, with an area under the receiver operating characteristic curve (AUC) of 0.985.[17]

External validation studies confirmed that the TBI had a very high sensitivity and specificity for detecting ECD.[40-47] Some studies, however, found a relatively lower sensitivity for detecting abnormality among eyes considered SCKC.[48-52] This could be explained by different criteria used to define SCKC,[53] including having normal tomography and biomechanics, based on BAD-D (Belin/Ambrósio Enhanced Ectasia Deviation)[37] and CBI (Corvis Corneal Biomechanical Index).[15] One must consider that some of these supposedly false-negative SCKC cases may truly represent patients with unilateral ectasia due to mechanical trauma such as eye rubbing.[54-57] Nevertheless, these findings support the unquestionable need for further enhancing the sensitivity to identify subclinical or mild ectasia cases.

The current study aimed to test if AI for integrating Scheimpflug tomography and biomechanical assessments could be upgraded or optimized by machine learning, using a more extensive population data set, thereby providing higher accuracy for ectasia detection.

METHODS

The current multicenter retrospective study followed the 1964 Declaration of Helsinki (revised in 2000). The institutional review board and human ethics committee of the Universidade Federal de São Paulo (UNIFESP, São Paulo, Brazil) approved this study.

- **PARTICIPANTS:** The study database comprised 3886unoperated eyes from 3412 patients. Twenty-five international centers contributed to the data collection. In a similar fashion to work accomplished in the development of the first version of the TBI,[17] the eyes were divided into 4 groups: normal patients (N), clinical "bilateral" KC patients, VAE-NT, and the VAE-E eyes from the patients with VAE. One eye was randomly selected from the N and KC groups. Both eyes of the patient with VAE entered the study unless the VAE-E eye had undergone any surgery (n = 1680 [N], 1181 [KC], 551 [VAE-NT], and 474 [VAE-E], respectively).

Every patient had a comprehensive ophthalmic examination, including the Corvis ST and Pentacam HR (Oculus Optikgeräte GmbH). As discussed below, only examinations with adequate quality for proper analysis were included. Patients were asked to suspend the use of soft contact lens wear for at least 1 week before the examination, and rigid or hybrid contact lenses were discontinued for a minimum period of 3 weeks. All cases had the Quad Refractive Map tomographic data blindly re-evaluated by a fellowship-trained expert (R.A.) on Cornea and Refractive Surgery to confirm the inclusion criteria.

The inclusion criterion for a normal subject (N) was a clinically unremarkable general eye examination in both eyes, including normal slitlamp biomicroscopy, distance-corrected visual acuity of 20/25 or better, normal Pentacam topometric findings, no previous surgery, and no use of topical medications different from artificial tears in both eyes. The diagnostic criterion for KC was clinical ectasia in both eyes without previous ocular surgeries.[58,59] The criteria for the diagnosis of corneal ectasia included topometric characteristics, such as skewed asymmetric bow-tie, inferior steepening, and at least 1 biomicroscopic slitlamp finding (Munson's sign, Vogt's striae, Fleischer's ring, apical thinning, Rizutti's sign).[59] VAE criteria were the diagnosis of ectasia in 1 eye based on the prior hitherto described criteria and the fellow eye being clinically normal based on normal biomicroscopy and a relatively normal front surface curvature (Pentacam topometric data).

All measurements with the Corvis ST and Pentacam HR were taken by experienced technicians considering previously reported protocols.[17] Proper examination quality was also assured by a manual, frame-by-frame analysis of each examination, made by an independent masked examiner to ensure the quality of each acquisition. The primary criterion for the Corvis ST measurement was good edge detection over the whole deformation response, excluding alignment errors (x-direction) and blinking errors. Pentacam HR and Corvis ST data were exported to a custom spreadsheet using special software. The Pentacam software version 1.21r59 and Corvis ST software version 1.6b2015 were used to extract an anonymous database containing 340 parameters from rotating Scheimpflug tomography and 90 parameters from the ultrahigh-speed Scheimplfug deformation response during noncontact tonometry.

- **ARTIFICIAL INTELLIGENCE OPTIMIZING PROTOCOL AND STATISTICS:** Different software tools performed statistical analyses and AI development: MedCalc Statistical Software version 16.8.4 (MedCalc, URL: https://www.medcalc.org/), SPSS version 23 (IBM Corp), the R-Core Team version 3.3.1.2016 (R Foundation for Statistical Computing, URL: https://www.R-project.org/), a custom-written MATLAB program (R14; The MathWorks), the Orange version 3.21.1 (University of Ljubljana, URL: https://orangedatamining.com/), and the Seaborn Python data visualization version 0.11.2 (http://seaborn.pydata.org/).

The data protection procedures included deidentifying the data by a computer server to store and process the data that were based on the TRIPOD (transparent reporting of a multivariable prediction model for individual prognosis or diagnosis) recommendations.[60] The data were analyzed and combined using different AI approaches using the "Knowledge Discovery in Databases" methodology.[61] The basic flow of steps for the data mining and the creation of the AI functions is summarized in Figure 1. The process goes from understanding the problem based on previous knowl-

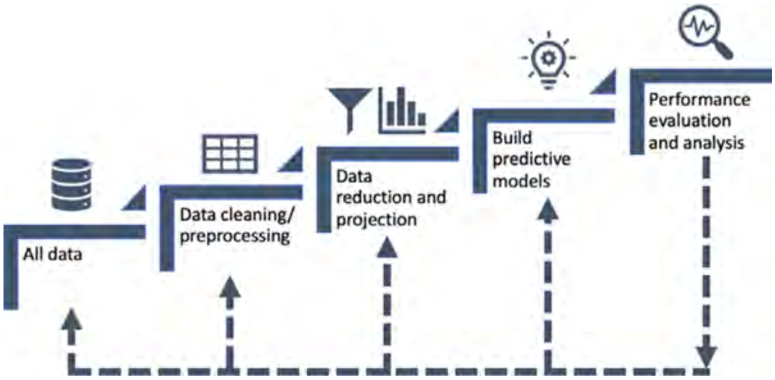

FIGURE 1. Basic flow of steps for the data mining and the creation of the artificial intelligence.

edge, feature selection, and creating different algorithms with cross-validation to validate the models. Then, these AI models are carefully analyzed and further refined to select the final best algorithm.

The first step was data cleaning and preprocessing. The initial data set has 430 attributes, including data related to the examination acquisition. Basic operations removed all irrelevant attributes with more than 40% of the same value, more than 40% of empty values, or with a variance of less than 0.09 among the patients. This step reduced the data set to 219 attributes. Then, the data sets from the original TBIv1 study (n = 778 patients; 850 eyes)[17] and from the first external validation, including cases from Rio de Janeiro (n = 487 patients; 544 eyes),[42] were separated. The remaining 2474 eyes from 2147 patients were divided into 2 subsets, training (2/3) and validation (1/3 eyes), for multiple iterations in the next step. Data reduction and projection were performed on training subsets using automatic feature selection techniques, such as forward selection, backward elimination, and genetic algorithms.[62] These methods were applied in a wrapper approach with the following machine learning algorithms: NN with multilayer perceptron (NN/MLP), k-nearest neighbors, decision tree (DT), logistic regression analysis (LRA), and RF. More than 1500 different attribute combinations were extracted as the next step considering or not including the TBIv1.

The next phase focused on the models that did not include the TBIv1 and applied those models to the complete data set. At this point, the goal was to build up and rank the predictive models based on the accuracy for ectasia detection. Each selected attribute combination was performed using the selected machine learning algorithm. The 10-fold cross-validation was chosen because of the larger population, decreasing computational time, and complexity. In this step, 790 predictive models were analyzed and ranked automatically based on the best AUC and sensitivity for detecting cases with VAE-NT. The top 15 models were selected and carefully analyzed for electing the best 5 models. Each model was carefully reviewed, considering the clinical relevance of the selected features. Finally, the set of features for each model was tested with different machine learning algorithms to define the best model based on the highest consistency and accuracy.

- **STATISTICAL ANALYSIS:** There were 3 types of analysis performed: normal vs "disease" (KC + VAE-E + VAE-NT), N vs clinical ectasia (KC + VAE-E), and N vs VAE-NT. First, the Shapiro-Wilk test checked for normal distributions. Considering that the distributions of the parameters in the KC group were non-normally distributed, the analyzed parameters were compared among the groups using the nonparametric Kruskal-Wallis test, followed by the post hoc Dunn's test to compare each pair of groups. Statistical significance was determined for a *P* value lower than .001.

The AUC was calculated for each parameter, considering the best cutoff value for the highest accuracy, determining sensitivity and specificity. Pairwise comparisons of the AUCs were accomplished with a nonparametric approach as described by DeLong and associates[63] to compare the performance of diagnostic tests. Separation curves that display accuracy as a function of shifting the cutoff value were plotted as described by Bühren and associates.[11] This method allows for comparisons among the different metrics using normalized cutoff points by a *Z* transformation in which the optimum cutoff is adjusted to zero. The area under the separation curve (AUSEP) calculates for the *y* limits of 50% and 100% accuracy, separating the *x* limits of −1 and 1 standard deviations. Thus, the AUSEP values indicate the tolerance to shifts on the cutoff criteria, which may evaluate the discriminatory ability of the parameter.[11] For receiver operating characteristic analysis, a custom-written MATLAB program (R14; the MathWorks) was used to confirm results obtained by MedCalc. All combined parameters were programmed to have their output values as a scale value ranging from zero to 1. An LRA function was created for the BAD-D to facilitate graphical comparisons.[17]

The correlations between the parameters were tested with Pearson's correlation coefficient (r) or Spearman's coefficient of rank correlation (ρ) accordingly to the distribution of the variables.

TABLE 1. Descriptive Statistics for Age

Group	N	Mean	SD	Median	Minimum	25th Percentile	75th Percentile	Maximum
Clinically normal	1680	34.19	13.69	30.37	6.99	24.45	41.00	90.06
KC	1181	31.59	11.18	29.59	6.64	23.67	37.18	78.39
VAE-E	474	31.03	12.74	27.88	10.34	21.88	37.44	83.15
VAE-NT	551	31.02	13.03	27.93	10.34	21.65	37.22	83.15

KC = keratoconic, VAE-E = ectatic unoperated eyes from the very asymmetric ectasia patients, VAE-NT = normal topography from very asymmetric ectasia patients.

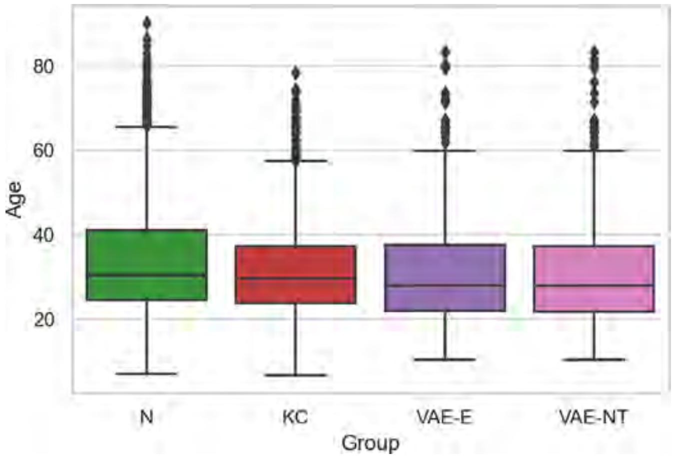

FIGURE 2. Descriptive statistics for age. KC = keratoconic, N = normal patient, VAE-E = ectatic unoperated eyes from the very asymmetric ectasia patients, VAE-NT = normal topography from very asymmetric ectasia patients.

RESULTS

Table 1 summarizes the age demographics. The mean age in the normal group was 34.2 years, and 31.6 and 31 years in the KC and VAE groups, respectively. There were significant differences in age (Kruskal-Wallis test, $P < .001$), with post hoc Dunn's analysis being significant for the differences with normal patients being older than the other groups ($P < .001$). However, such differences were considered of limited clinical significance, as shown in Figure 2.

The algorithm with the highest accuracy for enhancing ectasia detection was a novel RF algorithm, called the BrAIN-TBI (Brazilian Artificial Intelligence Networking in Medicine) or TBIv2. The TBIv2 included 18 features using 156 trees with 10-fold cross-validation. Table 2 summarizes the 18 features selected, including 10 parameters from rotating Scheipflug corneal tomography (Pentacam) and 8 parameters from corneal deformation response during noncontact tonometry (Corvis ST).

An LRA function was applied for the BAD-D version 3 (Belin/Ambrósio Enhanced Ectasia Deviation [v3]), so that it was normalized as an index, ranging from 0 to 1 (BAD-DI). The BAD-DI was ($y = a + b * x$): −4.02447 (constant) + (2.5203 * BAD-D). The BAD-D and BAD-DI had a perfect correlation (Spearman's coefficient of rank correlation; $P < .0001$; $\rho = 1.0$).

Figure 3 illustrates the scatterplot matrices of the most significant parameters plotted pairwisely: age, BAD-D, BAD-DI, PRFI (Pentacam Random Forest Index), stiffness parameter at first applanation, CBI, TBIv1, and TBIv2. Figure 4 presents the box/dot-plot distributions for the most relevant parameters in the 4 groups.

Table 3A, B, and C summarizes the AUC data, comparing the accuracy of the TBIv1,[17] the novel TBIv2, the PRFI,[16] the BAD-D,[37] and the CBI[15] for N × all (KC + VAE-E + VAE-NT), N × clinical ectasia (KC + VAE-E), and N × VAE-NT, respectively. For every pairwise comparison for every analysis, the RF parameters (TBIv1, TBIv2, and PRFI) had a statistically significant higher AUC than BAD-D and CBI (DeLong, $P < .001$). In addition, the BAD-D had a higher AUC than CBI for all studies (DeLong, $P < .001$).

For all cases (N × KC + VAE-E + VAE-NT), the TBIv1 had an AUC of 0.974, with 90% sensitivity and 96.2% specificity for a cutoff of 0.41. The AUC of the TBIv1 was 0.999 for discriminating clinical ectasia (KC and VAE-E), with 98.5% sensitivity and 98.6% specificity for a cutoff of

TABLE 2. The 18 Features Selected for the AI Algorithm of the TBIv2

Parameter	Origin	Definition
CBI	Corvis ST	Corvis Corneal Biomechanical Index
DARatioTMax2mm	Corvis ST	Ratio of the deformation amplitude at 2 mm
DensitoIncreaseMax	Corvis ST	The maximal change in backscattering of the cornea during the exam
HC Deformation Amp_mm	Corvis ST	Highest concavity deformation amplitude
MaxInverseRadius	Corvis ST	Minimal radius of curvature during the concave phase of deformation
PeakDist_mm	Corvis ST	Horizontal distance between the 2 highest points (nasal and temporal) of the cornea at the time of maximum deformation
SPA1	Corvis ST	Stiffness parameter at the first applanation
SPHC	Corvis ST	Stiffness parameter at the highest concavity
BADDb	Pentacam	Deviation from normality of the enhanced posterior elevation best-fit-sphere
BFSFront Thinnest 3mm	Pentacam	Best-fit sphere for anterior 3 mm centered at the thinnest point
ISValue	Pentacam	Inferior-superior axial steepening
KMaxFrontY	Pentacam	Vertical deviation of the point with maximal keratometry (Kmax) from the apex
Pac_Asymm_ApexVert8.0mm	Pentacam	Vertical asymmetry of the pachymetry at 8 mm
PRFI	Pentacam	Pentacam Random Forest Index
SphRMin	Pentacam	The minimal mean radius of a ring based on Fourier analysis (zero-order component)
TiltMinAxisMVP	Pentacam	Axis location of maximal decentration based on Fourier analysis (first-order wave component)
TiltMinMVP	Pentacam	The maximum decentration based on Fourier analysis (first-order wave component)
Ele. BBFTE 8mm @ Thinnest	Pentacam	Back (posterior) elevation at the thinnest point considering a best-fit toric ellipsoid for 8 mm

AI = artificial intelligence, TBI = tomographic and biomechanical index.

0.5. The AUC of the TBIv1 was 0.899 for VAE-NT, with 76% sensitivity and 89.1% specificity for an optimized cutoff of 0.29. For all cases, the TBIv2 had an AUC of 0.985, with 92.8% sensitivity and 97.4% specificity (cutoff: 0.65), which was higher than TBI (0.974; DeLong, $P < .0001$). The TBIv2 had a similar AUC for clinical ectasia (0.999; DeLong, $P = .818$; 98.7% sensitivity and 99.2% specificity [cutoff: 0.8]) but had a higher separation curve. The TBIv2 had a significantly higher AUC (0.945; DeLong, $P < .0001$) for detecting VAE-NT (84.4% sensitivity and 90.1% specificity [cutoff: 0.43]; DeLong, $P < .001$). The combination of these 18 features also performed well in an LRA with an AUC of 0.984, and an NN/MLP including these features had an AUC of 0.981 for all cases (N × KC + VAE-E + VAE-NT).

The study comparing normal vs all cases or "disease" (KC + VAE-E + VAE-NT) is summarized in Table 3A and Figure 5A. The TBIv2 had a significantly higher AUC than all other parameters (DeLong, $P < .0001$). The TBIv1 had a larger AUC (0.974) than PRFI (0.972) but with no statistical significance (DeLong, $P = .2979$). The AUSEP curves provided higher separation for the TBIv2 than the TBIv1 and PRFI (87, 82, and 68, respectively).

Table 3B and Figure 5B indicate the study to distinguish N from clinical ectasia cases (KC + VAE-E). The TBIv2, the TBIv1, and the PRFI had a similar AUC of 0.999 and the same 95% confidence intervals between 0.997 and 1. The AUC of the BAD-D was 0.995, which was statistically lower than the TBI and PRFI, but higher than the AUC of the CBI (0.968; DeLong, $P < .0001$).

The comparison of normal corneas vs the cases with VAE-NT is presented in Table 3C and Figure 5C. In these diverse cases, the difference in accuracy is more pronounced. The TBIv2 had a higher AUC (0.945) than all other parameters (DeLong, $P < .0001$). The TBIv1 had a larger AUC (0.899) than PRFI (0.893) but was not statistically significant (DeLong, $P = .299$). The AUSEP curves provided higher separation for the TBIv2 than the TBIv1 and PRFI (70, 58, and 36, respectively). The BAD-D had an AUC of 0.823, which was statistically lower than the TBIv1 and PRFI but higher than the AUC of the CBI (0.788; DeLong, $P < .0001$). The TBIv1 and TBIv2 had a very high positive correlation with ρ of 0.902 (95% confidence interval: 0.896-0.908; Spearman, $P < .0001$; Figure 6).

The Kruskal-Wallis test found statistically significant differences for the TBIv1, TBIv2, PRFI, BAD-D, and CBI for maximal axial keratometric value (Kmax), inferior-superior asymmetry value (IS-value), and Ambrósio's relational thickness to the meridian with maximal pachymetric increase (ART-max).[64] There was statistical significance for every parameter at each pairwise group comparison in post hoc Dunn ($P < .001$), unless for KC vs VAE-E in any parameter. Table 4 summarizes the descriptive statistics (median and range) for these parameters.

The BAD-D, the best cutoff for distinguishing normal corneas from all groups (KC + VAE-E + VAE-NT), was 1.82, with a sensitivity of 85.5% and a specificity of 97.7%. The BAD-DI cutoff of 0.63 provided similar accuracy. For detecting clinical ectasia (KC + VAE-E), the best cutoff of the BAD-D was 1.98 (BAD-DI of 0.72), with a sensitivity

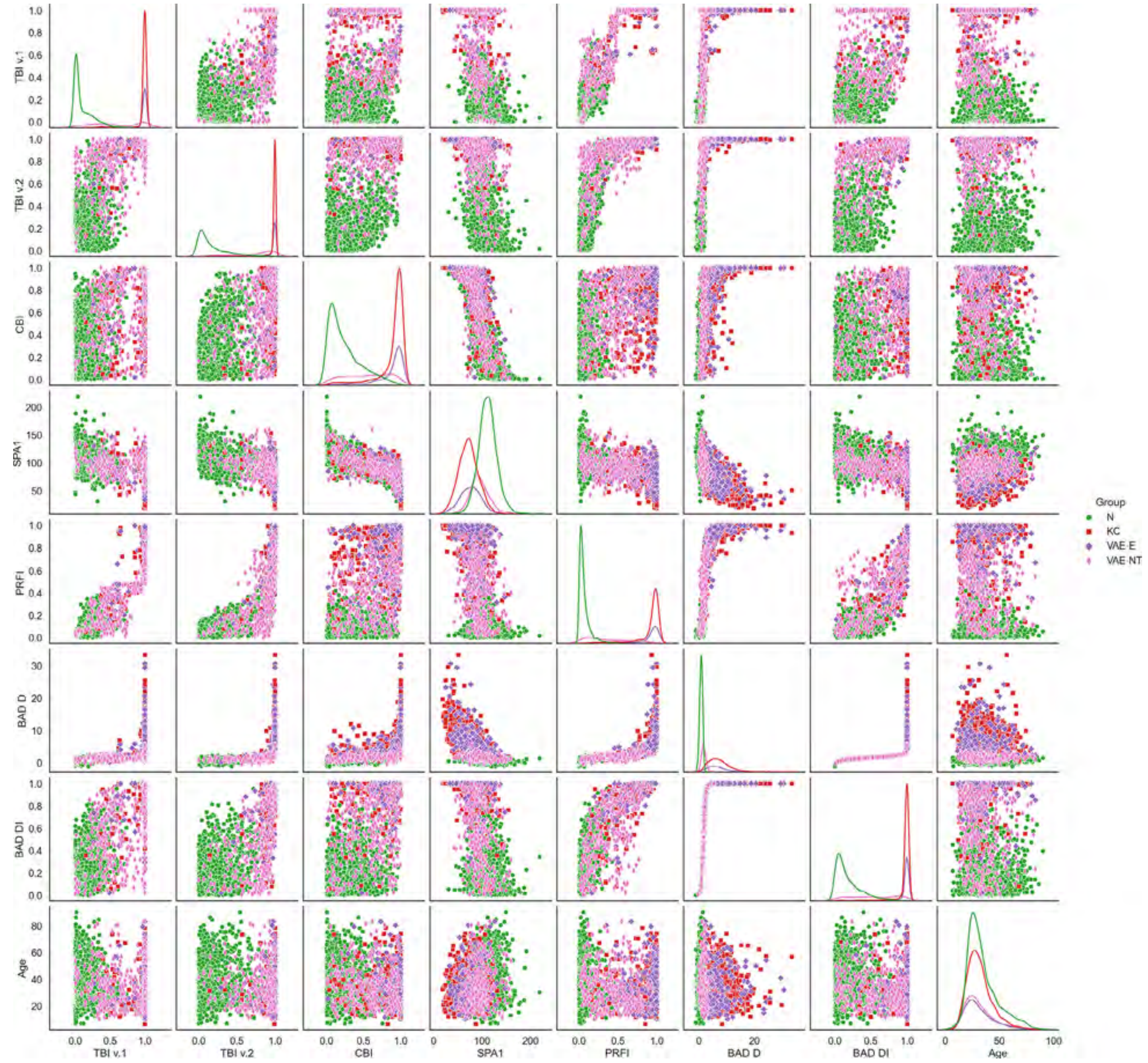

FIGURE 3. Scatterplot matrix of the first version of the tomographic and biomechanical index (TBIv1), the optimized version of the TBIv2, Pentacam random forest index (PRFI), Corvis biomechanical index (CBI), the stiffness parameter at first applanation (SPA1), Belin/Ambrósio Deviation (BAD-D), Belin/Ambrósio Deviation normalized index (BAD-DI), and age. KC = keratoconic, N = normal patient, VAE-E = ectatic unoperated eyes from the very asymmetric ectasia patients, VAE-NT = normal topography from very asymmetric ectasia patients.

of 96.8% and a specificity of 99.3%. The best cutoff for distinguishing the normal and the diverse VAE-NT group was 1.27 (BAD-DI of 0.31) with 70.8% sensitivity and 80.4% specificity. Interestingly, the cutoff of 1.6 (BAD-DI of 0.51), in which the parameter turns yellow in the BAD-D, would lead to 94% specificity and 98.4% sensitivity for clinical ectasia, but with a low sensitivity of 52.1% for the cases with VAE-NT.

In the original TBIv1 study,[17] objective criteria were rigorously applied for the cases with VAE-NT to be considered typical topometric data, including the KC percentage index (KISA%) lower than 60 and a paracentral IS-value at 6 mm (3 mm radii) less than 1.45D.[65] This criterion avoids recognized problems related to subjectivity and inter- and intra-examiner inconsistencies for the classifications of topometric maps.[66] Although 511 (92.7%) VAE-NT eyes obeyed such a criterion, there were 40 eyes from this group in the current study with objective topometric abnormalities. These cases were kept in the VAE-NT group as primarily selected SCKC because they were confirmed

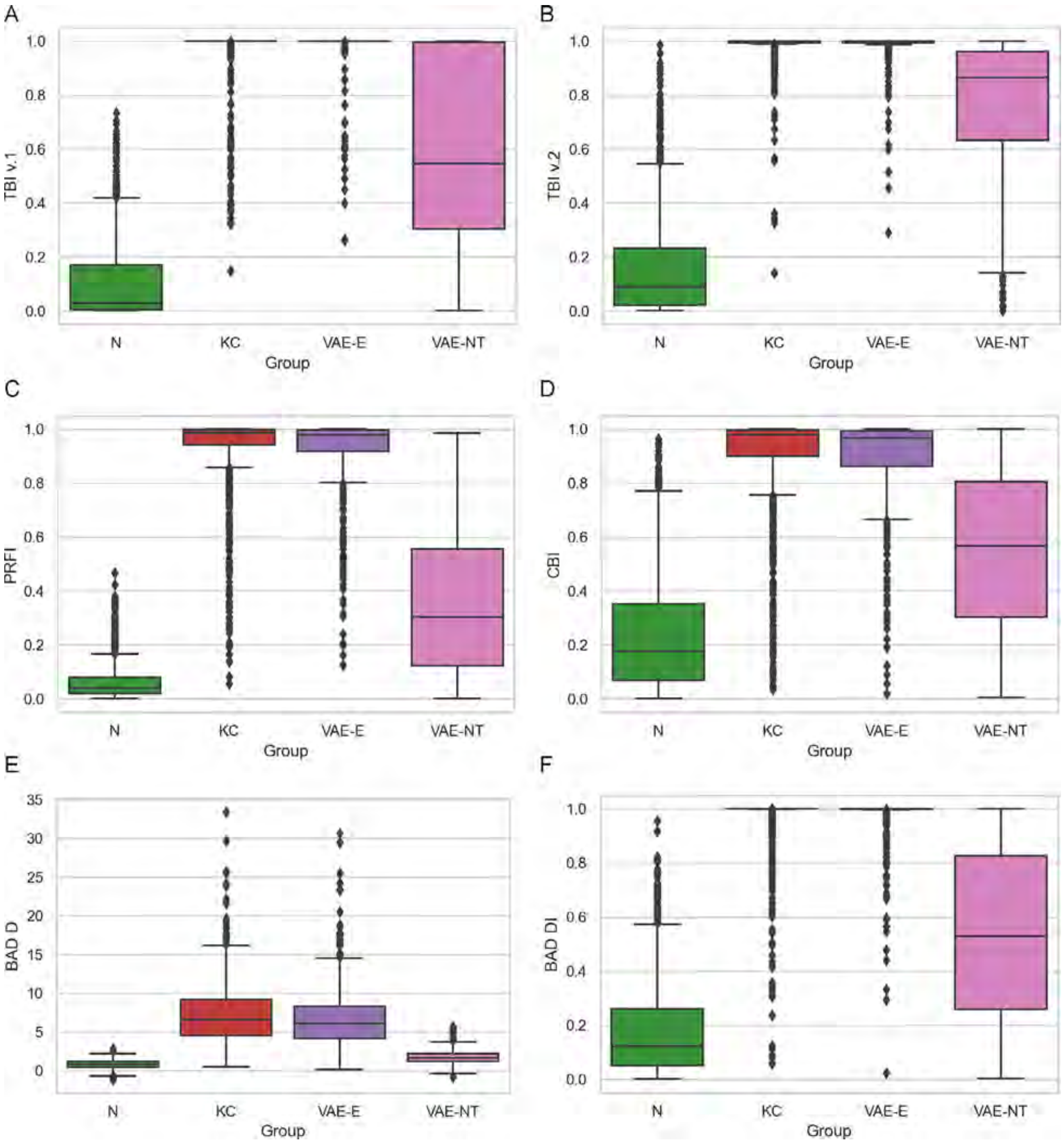

FIGURE 4. Box and dot plots showing the distribution of metric values across the groups (n = 1680 normal eyes [N], 1181 keratoconic eyes [KC], 551 eyes with normal topography from very asymmetric ectasia patients [VAE-NT], and 474 ectatic unoperated eyes from the very asymmetric ectasia patients [VAE-E]). A. The first version of the tomographic and biomechanical index (TBIv1). B. The optimized version of the TBIv2). C. Pentacam Random Forest Index (PRFI). D. Corvis Biomechanical Index (CBI). E. Belin/Ambrósio Deviation (BAD-D). F. Belin/Ambrósio Deviation normalized index (BAD-DI). The box spans the first and third quartile. The whiskers indicate the 1.5-fold interquartile range. Colored markers representing each value in each patient and its mean are superimposed.

to be the cases with VAE, considering the findings in the fellow VAE-E eye. Interestingly, accordingly to Rabinowitz and associates,[67] these cases are consistent with the criteria for FFKC.[35] From the 511 cases with VAE-NT with objectively typical topometric data, 75.1% had TBIv1 higher than 0.29 and 83.3% had TBIv2 higher than 0.43.

The asymmetry of the IS-value within 6 mm, as described by Rabinowitz,[59] with the classical cutoff value of

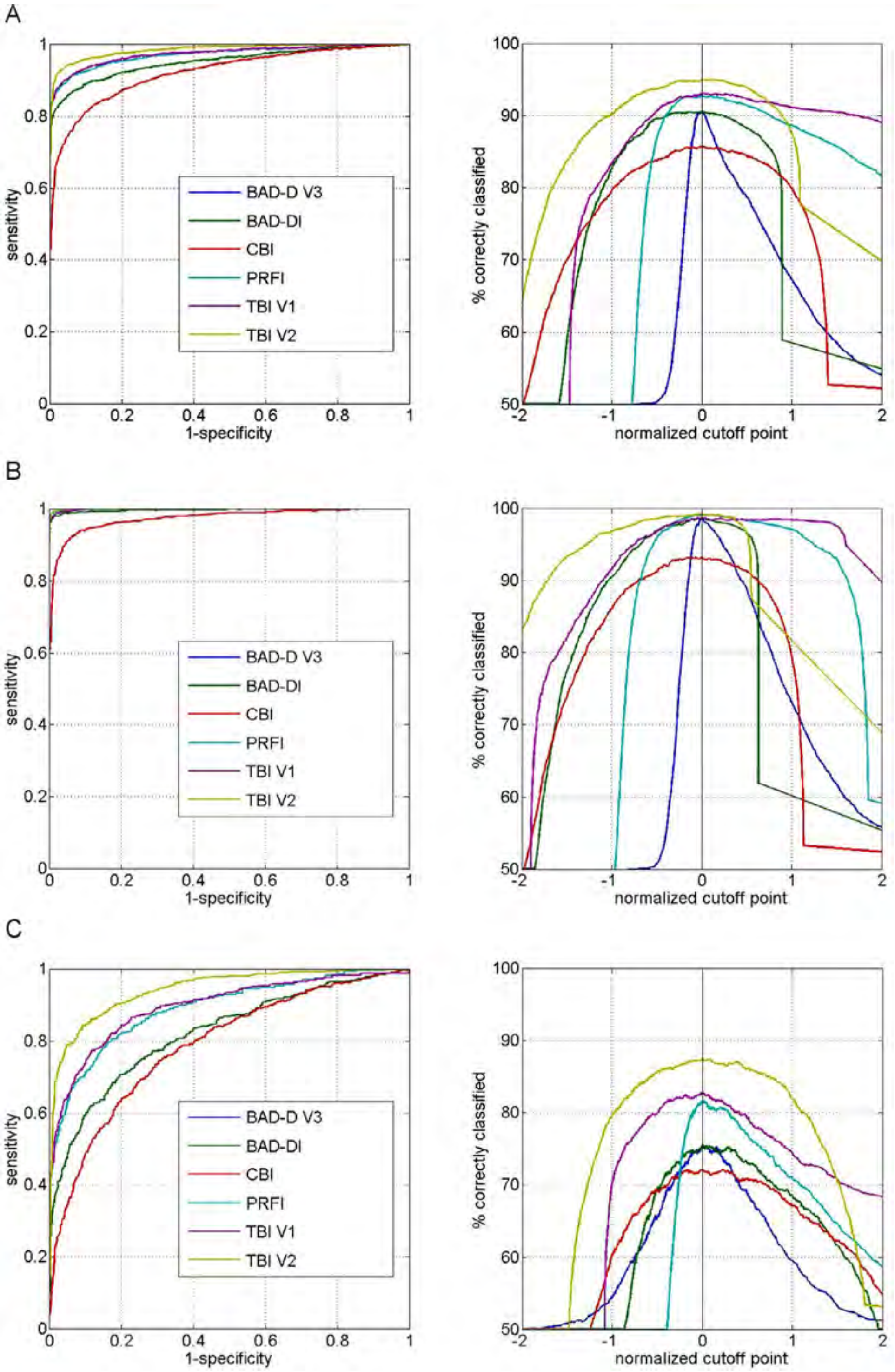

FIGURE 5. Receiver operating characteristic (ROC) and separation (SEP) curves for the different studies. A. Normal vs all groups (keratoconus [KC] + very asymmetric ectasia with clinical ectasia (VAE-E) + the normal topography eye from very asymmetric ectasia patients [VAE-NT]). B. Normal vs clinical ectasia (KC + VAE-E). C. Normal vs VAE-NT. BAD-D v3 = Belin/Ambrósio (version 3) Deviation, BAD-DI = Belin/Ambrósio Deviation normalized index, CBI = Corvis Biomechanical Index, PRFI = Pentacam Random Forest Index, TBI = tomographic and biomechanical index.

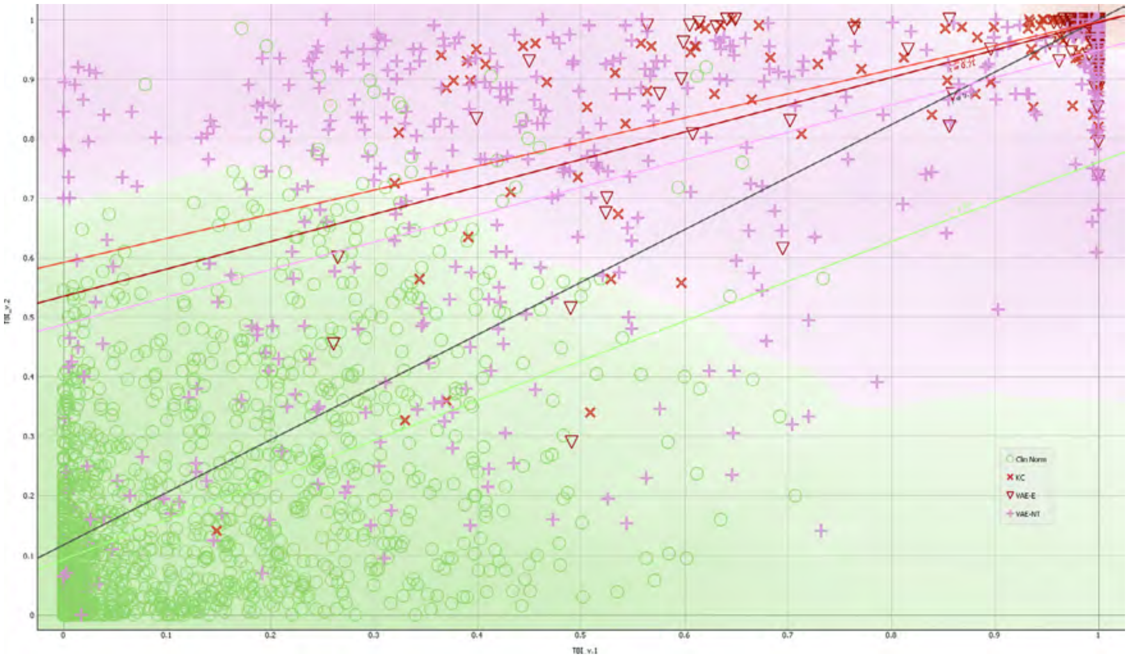

FIGURE 6. Correlation between the original (TBIv1) and the optimized version (TBIv2) of the tomographic and biomechanical index. KC = keratoconic, N = normal patient, VAE-E = ectatic unoperated eyes from the very asymmetric ectasia patients, VAE-NT = normal topography from very asymmetric ectasia patients.

1.6, would lead to a specificity of 99.6% and a sensitivity of 5.1% for the cases with VAE-NT and 84.5% for clinical ectasia. Reducing the cutoff to 1.45D, the specificity would decrease to 99.3%, with a sensitivity of 86.6% for clinical ectasia and 6.9% for the cases with VAE-NT. The Kmax with a cutoff value of 47.6D would lead to a specificity of 97.7% and a sensitivity of 82.1% for clinical ectasia and a sensitivity of 4.9% for the cases with VAE-NT. Interestingly, 8% of the clinical ectatic patients had a Kmax lower than 46D, and 3.3% had a Kmax lower than 45D. The ART-max,[64] with a cutoff value of 329 µm, has a specificity of 98% and a sensitivity of 93.7% for clinical ectasia but only 34.7% for VAE-NT. Considering the cutoff of 387 µm for ART-max, the specificity would decrease to 83.6%, with a sensitivity of 65.7% for VAE-NT.

DISCUSSION

The current multicenter cross-sectional case-control retrospective study demonstrated the ability to optimize AI algorithms integrating Scheimpflug-based corneal tomographic and biomechanical data to enhance ectasia detection. AI has the capacity to (and should) continuously evolve, boosting its complexity to improve accuracy.[7,68] AI improvements occur through better training, which necessitates more data for the refinements. The "Knowledge Discovery in Databases" process was applied for data mining and developing AI functions.[61] Feature selection techniques included forward selection, backward elimination, and genetic algorithms.[62] There are 2 ways to gather more information for the training protocols: larger population data sets and novel attributes or parameters.[2,7,68] We analyzed 3886 eyes from 3412 patients, considering 340 parameters extracted from the Pentacam and Corvis ST examinations.

Besides an extensive population data set, including a relatively large set of subclinical cases was a major reason for the success in optimizing AI training in this study. Including such cases allows for identifying nuances in the very mild, asymptomatic cases. In this context, patients presenting with VAE, in which the fellow eye had a comprehensive ophthalmic examination within normal limits, have served as the most common models to develop, test, and demonstrate the improved ability to detect ECD by using advanced imaging data.[7,12,13,17,19,36,37,69] Other inclusion criteria that could represent subclinical ectasia cases include the retrospective analysis of the preoperative state of eyes that developed progressive ectasia after LVC procedures[16] and longitudinal studies that identify the relatively normal cases with natural ectasia evolution.[55,70,71]

The first version of the TBI training set included 94 VAE-NT eyes, from which 85 (90.4%) had TBIv1 higher than 0.29.[17] The current study included 551 patients with VAE, with 511 within the rigorous, objective criteria for VAE-N: KISA less than 60 and IS-value lower than 1.45D.[65] In this more extensive series of cases with VAE-NT, the sensitivity

TABLE 3. Description of the AUC and AUSEP Curves Calculated Between the Limits of −1 and +1 Standard Deviations for (A) Normal vs All Groups (KC + VAE-E + VAE-NT], (B) Normal vs Clinical Ectasia (KC + VAE-E), and (C) Normal vs VAE-NT

Variable	AUC	SE	95% CI	AUSEP
(A) KC + VAE-E + VAE-NT				
TBIv1	0.974	0.00236	0.968-0.979	82
TBIv2	0.985	0.00156	0.981-0.989	87
PRFI	0.972	0.00239	0.967-0.977	68
BAD-D	0.952	0.00336	0.945-0.959	72
CBI	0.923	0.00418	0.914-0.931	68
(B) KC + VAE-E				
TBIv1	0.999	0.000269	0.997-1.000	93
TBIv2	0.999	0.000339	0.997-1.000	75
PRFI	0.999	0.000326	0.997-1.000	87
BAD-D	0.995	0.00114	0.992-0.997	75
CBI	0.968	0.00283	0.962-0.974	81
(C) KC + VAE-NT				
TBIv1	0.899	0.00861	0.886-0.911	58
TBIv2	0.945	0.00574	0.935-0.954	70
PRFI	0.893	0.00862	0.879-0.905	36
BAD-D	0.823	0.0112	0.807-0.839	38
CBI	0.788	0.0116	0.771-0.805	39

AUC = area under the receiver operating characteristic curve, AUSEP = area under the separation curve, BAD-D v3 = Belin/Ambrósio (version 3) Deviation, CBI = Corvis Biomechanical Index, KC = keratoconic, PRFI = Pentacam Random Forest Index, TBI = tomographic and biomechanical index, VAE-E = very asymmetric ectasia with clinical ectasia, VAE-NT = normal topography from very asymmetric ectasia patients.

SE, calculated by Bimonial exact; 95% CI, calculated based on DeLong's method.[59]

of the TBIv1 for the same cutoff of 0.29 was 76%. The new TBIv2 augmented the sensitivity up to 84.4% (DeLong, $P < .0001$).

The higher accuracy of the TBIv2 over the TBIv1[17] and the PRFI[16] could not be shown by the ability to detect clinical ectasia. Either TBIv1, TBIv2, and PRFI had a similar AUC of 0.999 with no statistical significance (DeLong, $P = .818$). The TBIv2 had a slight advantage in accuracy, with 98.7% sensitivity, 99.2% specificity, and a cutoff of 0.8. The TBIv1 had 98.5% sensitivity, 98.6% specificity, and a cutoff of 0.5. Paradoxically, the AUSEP of the TBIv2 was lower, which may be related to the higher cutoff. Also, although TBIv2 had a higher specificity, more normal cases had higher values (Figure 4). The interpretation for the high TBIv2 scores in some eyes in the clinically normal group is that those cases may have a higher susceptibility to developing ectasia, which can be tested in future prospective studies using finite element simulations.[31] Considering all cases, the TBIv2 also had a higher AUC (0.985) than the TBIv1 (0.974; DeLong, $P < .0001$) and PRFI (0.972; DeLong, $P < .0001$).

A significant limitation of this study is related to the fact that the cases with VAE represent a diverse group because some may be genuine cases with unilateral ectasia.[54-57,71,72] According to Global Consensus from 2015, KC is, by definition, an asymmetric bilateral disease, while secondary mechanical-related ectasia may occur in only 1 eye. In addition, the 2015 consensus failed to reach an agreement on the definition of FFKC.[58] Nevertheless, the concept that FFKC remains with high ectasia susceptibility, but did not progress to the disease's full-blown (forme pleine) presentation.[73] Although there is a significant variability in the criteria for defining SCKC and FFKC in the literature, the VAE-NT group may represent a logical group to test the ability of any parameter to quantify the level of predisposition or susceptibility for corneal biomechanical decompensation.[55,69,74] Another limitation of the current study was

TABLE 4. Descriptive Median and Range (Minimum to Maximum) for the Main Parameters

	Clinically Normal (n = 1680)			KC (n = 1181)			VAE-E (n = 474)			VAE-NT (n = 551)		
	Minimum	Median	Maximum	Minimum	Median	Maximum	Minimum	Median	Maximum	Minimum	Median	Maximum
TBIv1	0	0.028	0.734	0.148	1	1	0.261	1	1	0	0.546	1
TBIv2	0	0.09	0.985	0.141	1	1	0.29	1	1	0	0.865	1
PRFI	0	0.038	0.466	0.054	0.986	1	0.124	0.978	1	0	0.302	0.986
BAD-D (v3)	−1.13	0.81	2.81	0.49	6.64	33.42	0.1	6.105	30.63	−0.82	1.64	5.65
CBI	0	0.175	0.964	0.035	0.979	1	0.019	0.967	1	0.003	0.566	1
IS-value (D)	−1.63	0.11	2.16	−2.87	4.66	29.68	−7.08	3.85	19.84	−1.49	0.6	4.3.
Kmax (D)	39.6	44.5	49.8	41.5	52.3	85.1	42.5	51.6	86.2	38.9	44.7	55.1
ART-max (μm)	267	454	786	0	176	720	0	196	467	126	362	638

ART-max = Ambrósio's relational thickness to the maximal progression meridian, BAD-D = Belin/Ambrósio Deviation (version 3), CBI = Corvis Biomechanical Index, IS-value = the inferior-superior asymmetry at 6 mm in diameter, Kmax = maximal keratometric (axial) value on the front surface, PRFI = Pentacam Random Forest Index, TBIv1 = original tomographic and biomechanical index, TBIv2= optimized version of the tomographic and biomechanical index.

not to include less common phenotypes of "natural" ectasia: pellucid marginal degeneration and keratoglobus.[75] Still, these cases have typical presentations that may facilitate clinical diagnosis; there is a need for future studies testing the accuracy of the novel TBIv2 for detecting such cases.

The BrAIN-TBI or TBIv2 was the most consistent AI algorithm using a novel RF, including 18 features (Table 2) in 156 trees with 10-fold cross-validation. The parameters that were selected had relatively high clinical relevance. Rotating Scheimpflug tomography (Pentacam) [76,37] provided 10 features, and 8 parameters were derived from Corvis ultrahigh-speed Scheimpflug imaging during the noncontact tonometry.[77,78] The Pentacam parameters included the PRFI,[16] the paracentral IS-value at 6 mm (3 mm radii),[65] 3 metrics from corneal wavefront,[11] 1 metric from peripheral vertical pachymetric asymmetry,[79,80] the vertical deviation of the Kmax, 2 metrics from Belin's enhanced back elevation, and 1 metric from anterior elevation.[81-83] The CBI,[15] Roberts's stiffness parameters (at first applanation and at highest concavity momentum),[84,85] and other corneal deformation parameters were included.[77,78]

RF is an advanced compound method that involves multiple DT. As in a classic DT, the analyzed case is successively split into 2 mutual subgroups (branches) that subdivide until a final decision on class assignment (leaves). The RF approach considers numerous trees for a cooperative effort for the decision output. The algorithm grows the trees by sampling the data into random subgroups. Some input variables are also randomly selected to test the data splitting at each node. According to an objective function, the predictor variable that delivers the best split is applied to each node. Each tree gets a "vote" in the classification process. The final classification is based on the votes of all trees for providing a combined value that typically varies from zero to 1.[86]

The consistency of the model is highlighted because both the NN/MLP and LRA algorithms employing the same 18 variables had equally good diagnostic performances. As an iteration process, the RF model with these 18 variables trained with LOOCV had a slightly better AUC of 0.987 for all cases (N × KC + VAE-E + VAE-NT) but with no statistical significance (DeLong, $P = .169$). As for any machine learning method, it is fundamental to include a cross-validation method to minimize the risk of overfitting. Proper cross-validation will infer or presume the ability to generalize the external validity of the model. The first version of the TBI used LOOCV.[17] In contrast, the current study employed 10-fold cross-validation because of the larger population as it decreases computational time and complexity, still maintaining and possibly enhancing generalization. By this means, the 10-fold cross-validation ensures the reliability or robustness of the model for classifying new data. Unlike LOOCV, the database is randomly divided into 10 groups, balancing the number of cases in the subgroups. Subsequently, the AI training of the model has repeated 10 folds. Each time, one group is excluded, in which the model trained with the 9 of 10 cases is tested. The reported outcomes of the TBIv2 include the outputs from the 10-fold cross-validation model. These results present a lower (less optimistic) accuracy when compared with the virtually perfect accuracy of the final TBIv2 model that contemplates all cases and will be programmed in the commercial Oculus software (Ambrósio, Roberts & Vinciguerra Tomography and Biomechanical Display). However, the cross-validation results are expected to represent a more trustworthy picture of the expected generalized performance for the TBIv2 in clinical application.

The last 3 decades witnessed a tremendous advance in corneal imaging, which includes the development of high-resolution technologies capable of detailed characterizations of different aspects of corneal shape and anatomy and introducing scientifically validated methods for representing and interpreting the generated data.[87] Applying AI was a natural progression for analyzing the overwhelming plethora of available data.[7,8,54]

Placido disk–based corneal topography characterizes the anterior or front corneal surface, enabling the detection of abnormalities consistent with mild-to-moderate forms of KC in eyes with normal slitlamp biomicroscopy and normal distance-corrected visual acuity.[88,89] There are still cases that develop ectasia despite relatively normal preoperative topography before laser in situ keratomileusis (LASIK),[30,90-92] SmILE (small incision lenticular extraction),[93,94] surface ablation,[95] and even LASIK-Xtra (LASIK with prophylactic crosslinking).[96] Ectasia detection is also relevant when evaluating candidates for refractive cataract surgery,[97] because it impacts intraocular lens calculation, quality of vision, and the ability for corneal enhancements.[98,99]

Front surface corneal topography evolved into 3-dimensional tomographic analysis, which characterizes the front (including topometric or curvature) and back surfaces' elevation and thickness mapping.[100] Further advances in corneal imaging allowed for segmental or layered tomographic (3-dimensional) characterization with epithelial thickness[14,101-103] and Bowman's layer mapping.[20,104,105] Beyond shape analysis, in the context of multimodal refractive imaging,[8] clinical biomechanical assessment has been considered an additional tool for augmenting the sensitivity for identifying mild forms of ECD and the characterization of the inherent susceptibility for ectasia progression.[17,53,106,107] Future biomechanical assessment to characterize material stiffness using Corvis ST data (ie, stress-strain index map)[108] or from novel tools such as Brillouin microscopy[109-113] and phase-decorrelation ocular coherence tomography[109,114-116] may further enhance AI applications. Ultimately, genetic testing through linkage analysis or genome-wide association studies may further elucidate about the intrinsic susceptibility for biomechanical decompensation, which promises to test and further improve AI for ectasia diagnosis.[117-119]

This study was limited to patients with unoperated corneas. Future external validation studies are needed to test the accuracy of the TBIv2, including testing the specificity among cases with high astigmatism, corneal warpage, and dry eye. Further AI optimization is expected for post-LVC procedures, as developed by Vinciguerra and associates[120] for the CBI after LVC. In addition, specific improvements for certain ethnicities (ie, Chinese and Sub-Saharan Africa) can augment specificity while not jeopardizing the model's sensitivity. Besides diagnosis, AI can be developed to improve prognosis and clinical follow-up, as described by integrating biomechanical parameters into Belin's tomographic ABCD system.[121-123] The relevance for enhanced ectasia detection may go beyond the management of cases with ECD and assessing ectasia risk before elective LVC procedures. For example, there are different associations of KC with posterior segment structure findings (ie, optic nerve head and the choroid).[124] In addition, the hypothesis that mild or SCKC could be a risk factor for a mother to have a baby with Down's syndrome was also raised.[125] Although understanding the underlying mechanisms for such relationships is not complete, enhanced analysis of the cornea based on properly trained AI, considering specific well-designed fundamental questions, may provide relevant parameters for future clinical applications.

The current study validated the hypothesis that AI can be optimized to improve ectasia detection. Such advances may augment the reliability of clinical decisions related to screening cases at risk for ectasia after LVC. The relevance of AI develops fast in different areas of ophthalmology. We predict rapid developments with increasing applications for enhancing the safety and efficiency of therapeutic and elective refractive surgery. AI advances should involve gathering extensive data from large populations and including features from multimodal imaging technologies, such as epithelial thickness (segmental or layered tomography), axial length, and ocular wavefront data.

ALL AUTHORS ATTEST THAT THEY MEET THE CURRENT ICMJE CRITERIA FOR AUTHORSHIP. THE OTHER AUTHORS HAVE NO CONFLICT OF INTEREST TO DISCLOSE.
Funding/Support: This study received no funding. Financial Disclosures: R.A., P.V., R.V., C.J.R., B.L., M.W.B., A.E., and J.B. are consultants for Oculus Optikgeräte GmbH (Wetzlar, Germany).
Acknowledgments: The authors thank Dr Sven Reisdorf, Stefanie Berger, and Niklas Schmidt (Oculus Optikgeräte GmbH) for their valuable data processing, helpful discussions, and statistical calculations.

REFERENCES

1. Wilson SE, Klyce SD. Advances in the analysis of corneal topography. *Surv Ophthalmol*. 1991;35(4):269–277.
2. Kapoor R, Walters SP, Al-Aswad LA. The current state of artificial intelligence in ophthalmology. *Surv Ophthalmol*. 2019;64(2):233–240.
3. Abramoff MD, Tobey D, Char DS. Lessons learned about autonomous AI: finding a safe, efficacious, and ethical path through the development process. *Am J Ophthalmol*. 2020;214:134–142.
4. Chiang M, Guth D, Pardeshi AA, et al. Glaucoma expert-level detection of angle closure in goniophotographs with convolutional neural networks: the Chinese American Eye Study. *Am J Ophthalmol*. 2021;226:100–107.
5. Cheng H, Wang L, Kane JX, Li J, Liu L, Wu M. Accuracy of artificial intelligence formulas and axial length adjustments for highly myopic eyes. *Am J Ophthalmol*. 2021;223:100–107.
6. Keenan TDL, Chakravarthy U, Loewenstein A, Chew EY, Schmidt-Erfurth U. Automated quantitative assessment of retinal fluid volumes as important biomarkers in neovascular age-related macular degeneration. *Am J Ophthalmol*. 2021;224:267–281.
7. Lopes BT, Eliasy A, Ambrosio R. Artificial intelligence in corneal diagnosis: where are we? *Curr Ophthalmol Rep*. 2019;7(3):204–211.
8. Ambrosio Jr R. Multimodal imaging for refractive surgery: Quo vadis? *Indian J Ophthalmol*. 2020;68(12):2647–2649.
9. Maeda N, Klyce SD, Smolek MK. Neural network classification of corneal topography. Preliminary demonstration. *Invest Ophthalmol Vis Sci*. 1995;36(7):1327–1335.
10. Smolek MK, Klyce SD. Current keratoconus detection methods compared with a neural network approach. *Invest Ophthalmol Vis Sci*. 1997;38(11):2290–2299.
11. Bühren J, Kuhne C, Kohnen T. Defining subclinical keratoconus using corneal first-surface higher-order aberrations. *Am J Ophthalmol*. 2007;143(3):381–389.
12. Arbelaez MC, Versaci F, Vestri G, Barboni P, Savini G. Use of a support vector machine for keratoconus and subclinical keratoconus detection by topographic and tomographic data. *Ophthalmology*. 2012;119(11):2231–2238.
13. Smadja D, Touboul D, Cohen A, et al. Detection of subclinical keratoconus using an automated decision tree classification. *Am J Ophthalmol*. 2013;156(2):237–246 e231.
14. Silverman RH, Urs R, Roychoudhury A, Archer TJ, Gobbe M, Reinstein DZ. Epithelial remodeling as basis for machine-based identification of keratoconus. *Invest Ophthalmol Vis Sci*. 2014;55(3):1580–1587.
15. Vinciguerra R, Ambrósio Jr R, Elsheikh A, et al. Detection of keratoconus with a new biomechanical index. *J Refract Surg*. 2016;32(12):803–810.
16. Lopes BT, Ramos IC, Salomao MQ, et al. Enhanced tomographic assessment to detect corneal ectasia based on artificial intelligence. *Am J Ophthalmol*. 2018;195:223–232.
17. Ambrosio Jr R, Lopes BT, Faria-Correia F, et al. Integration of Scheimpflug-based corneal tomography and biomechanical assessments for enhancing ectasia detection. *J Refract Surg*. 2017;33(7):434–443.
18. Klyce SD. The future of keratoconus screening with artificial intelligence. *Ophthalmology*. 2018;125(12):1872–1873.

19. Hwang ES, Perez-Straziota CE, Kim SW, Santhiago MR, Randleman JB. Distinguishing highly asymmetric keratoconus eyes using combined Scheimpflug and spectral-domain OCT analysis. *Ophthalmology*. 2018;125(12):1862–1871.
20. Chandapura R, Salomao MQ, Ambrosio Jr R, Swarup R, Shetty R, Sinha Roy A. Bowman's topography for improved detection of early ectasia. *J Biophotonics*. 2019;12(10):e201900126.
21. Maile H, Li JO, Gore D, et al. Machine learning algorithms to detect subclinical keratoconus: systematic review. *JMIR Med Inform*. 2021;9(12):e27363.
22. Kanellopoulos AJ. Keratoconus management with customized photorefractive keratectomy by artificial intelligence ray-tracing optimization combined with higher fluence corneal crosslinking: the ray-tracing Athens protocol. *Cornea*. 2021;40(9):1181–1187.
23. Atalay E, Ozalp O, Yildirim N. Advances in the diagnosis and treatment of keratoconus. *Ther Adv Ophthalmol*. 2021;13:25158414211012796.
24. Malyugin B, Sakhnov S, Izmailova S, et al. Keratoconus diagnostic and treatment algorithms based on machine-learning methods. *Diagnostics (Basel)*. 2021;11(10):1933.
25. McGhee CN, Kim BZ, Wilson PJ. Contemporary treatment paradigms in keratoconus. *Cornea*. 2015;34(suppl 10):S16–S23.
26. Ambrósio R, Lopes B, Amaral J, et al. Keratoconus: breaking paradigms and contradictions of a new subspecialty. *Rev Bras Oftalmol*. 2019;78:81–85.
27. Binder PS, Lindstrom RL, Stulting RD, et al. Keratoconus and corneal ectasia after LASIK. *J Refract Surg*. 2005;21(6):749–752.
28. Ambrosio Jr R, Randleman JB. Screening for ectasia risk: what are we screening for and how should we screen for it? *J Refract Surg*. 2013;29(4):230–232.
29. Ambrósio Jr R, Belin M. Enhanced screening for ectasia risk prior to laser vision correction. *Int J Keratoconus Ectatic Corneal Dis*. 2017;6(1):23–33.
30. Ambrósio Jr R. Post-LASIK ectasia: twenty years of a conundrum. *Semin Ophthalmol*. 2019;34(2):66–68. doi:10.1080/08820538.2019.1569075.
31. Dupps Jr WJ, Seven I. A large-scale computational analysis of corneal structural response and ectasia risk in myopic laser refractive surgery. *Trans Am Ophthalmol Soc*. 2016;114:T1.
32. Francis M, Khamar P, Shetty R, et al. In vivo prediction of air-puff induced corneal deformation using LASIK, SMILE, and PRK finite element simulations. *Invest Ophthalmol Vis Sci*. 2018;59(13):5320–5328.
33. Roberts CJ, Dupps Jr WJ. Biomechanics of corneal ectasia and biomechanical treatments. *J Cataract Refract Surg*. 2014;40(6):991–998.
34. Klyce SD. Chasing the suspect: keratoconus. *Br J Ophthalmol*. 2009;93(7):845–847.
35. Henriquez MA, Hadid M, Izquierdo Jr L. A systematic review of subclinical keratoconus and forme fruste keratoconus. *J Refract Surg*. 2020;36(4):270–279.
36. Saad A, Gatinel D. Topographic and tomographic properties of forme fruste keratoconus corneas. *Invest Ophthalmol Vis Sci*. 2010;51(11):5546–5555.
37. Ambrosio Jr R, Valbon BF, Faria-Correia F, Ramos I, Luz A. Scheimpflug imaging for laser refractive surgery. *Curr Opin Ophthalmol*. 2013;24(4):310–320.
38. Golan O, Piccinini AL, Hwang ES, et al. Distinguishing highly asymmetric keratoconus eyes using dual Scheimpflug/placido analysis. *Am J Ophthalmol*. 2019;201:46–53.
39. Mahmoud AM, Nunez MX, Blanco C, et al. Expanding the cone location and magnitude index to include corneal thickness and posterior surface information for the detection of keratoconus. *Am J Ophthalmol*. 2013;156(6):1102–1111.
40. Sedaghat M-R, Momeni-Moghaddam H, Ambrósio Jr R, et al. Diagnostic ability of corneal shape and biomechanical parameters for detecting frank keratoconus. *Cornea*. 2018;37(8):1025–1034.
41. Kataria P, Padmanabhan P, Gopalakrishnan A, Padmanaban V, Mahadik S, Ambrósio Jr R. Accuracy of Scheimpflug-derived corneal biomechanical and tomographic indices for detecting subclinical and mild keratectasia in a South Asian population. *J Cataract Refract Surg*. 2019;45(3):328–336.
42. Ferreira-Mendes J, Lopes BT, Faria-Correia F, Salomão MQ, Rodrigues-Barros S, Ambrósio Jr R. Enhanced ectasia detection using corneal tomography and biomechanics. *Am J Ophthalmol*. 2019;197:7–16.
43. Salomao MQ, Hofling-Lima AL, Gomes Esporcatte LP, et al. The role of corneal biomechanics for the evaluation of ectasia patients. *Int J Environ Res Public Health*. 2020;17(6):2113.
44. Fernandez J, Rodriguez-Vallejo M, Pinero DP. Tomographic and biomechanical index (TBI) for screening in laser refractive surgery. *J Refract Surg*. 2019;35(6):398.
45. Liu Y, Zhang Y, Chen Y. Application of a Scheimpflug-based biomechanical analyser and tomography in the early detection of subclinical keratoconus in Chinese patients. *BMC Ophthalmol*. 2021;21(1):339.
46. Zhang M, Zhang F, Li Y, Song Y, Wang Z. Early diagnosis of keratoconus in Chinese myopic eyes by combining Corvis ST with Pentacam. *Curr Eye Res*. 2020;45(2):118–123.
47. Augustin VA, Son HS, Baur I, Zhao L, Auffarth GU, Khoramnia R. Detecting subclinical keratoconus by biomechanical analysis in tomographically regular keratoconus fellow eyes. *Eur J Ophthalmol*. 2021 11206721211063740. doi:10.1177/11206721211063740.
48. Steinberg J, Siebert M, Katz T, et al. Tomographic and biomechanical Scheimpflug imaging for keratoconus characterization: a validation of current indices. *J Refract Surg*. 2018;34(12):840–847.
49. Chan TCY, Wang YM, Yu M, Jhanji V. Comparison of corneal tomography and a new combined tomographic biomechanical index in subclinical keratoconus. *J Refract Surg*. 2018;34(9):616–621.
50. Koh S, Ambrosio Jr R, Inoue R, Maeda N, Miki A, Nishida K. Detection of subclinical corneal ectasia using corneal tomographic and biomechanical assessments in a Japanese population. *J Refract Surg*. 2019;35(6):383–390.
51. Koc M, Aydemir E, Tekin K, Inanc M, Kosekahya P, Kiziltoprak H. Biomechanical analysis of subclinical keratoconus with normal topographic, topometric, and tomographic findings. *J Refract Surg*. 2019;35(4):247–252.
52. Fraenkel D, Hamon L, Daas L, et al. Tomographically normal partner eye in very asymmetrical corneal ectasia: biomechanical analysis. *J Cataract Refract Surg*. 2021;47(3):366–372.
53. Esporcatte LPG, Salomão MQ, Lopes BT, et al. Biomechanical diagnostics of the cornea. *Eye Vis (Lond)*. 2020;7(1):9.

54. Salomão M, Hoffling-Lima AL, Lopes B, et al. Recent developments in keratoconus diagnosis. *Expert Rev Ophthalmol.* 2018;13(6):329–341.
55. Salomão MQ, Hofling-Lima AL, Esporcatte LPG, et al. Ectatic diseases. *Exp Eye Res.* 2021;202:108347.
56. Kansal V, Ambrósio Jr R, Sharma V. Unilateral traumatic posterior corneal ectasia: clinical manifestations, findings of advanced imaging, and long-term follow-up. *J Refract Surg.* 2021;1(3):e31–e35.
57. Criado GG, Júnior NBS, Mazzeo TJMM, et al. Caracterização de ectasia subclínica com análise integrada da tomografia e biomecânica da córnea. Article in Portuguese. *Rev Bras Oftalmol.* 2021;80(1):71–76.
58. Gomes JA, Tan D, Rapuano CJ, et al. Global consensus on keratoconus and ectatic diseases. *Cornea.* 2015;34(4):359–369.
59. Rabinowitz YS. Keratoconus. *Surv Ophthalmol.* 1998;42(4):297–319.
60. Collins GS, Reitsma JB, Altman DG, Moons KG. Transparent reporting of a multivariable prediction model for individual prognosis or diagnosis (TRIPOD): the TRIPOD statement. *BMC Med.* 2015;13:1.
61. Fayyad U, Piatetsky-Shapiro G, Smyth P. From data mining to knowledge discovery in databases. *AI Magazine..* 1996;17(3):37.
62. Khalid S, Khalil T, Nasreen S. A survey of feature selection and feature extraction techniques in machine learning. In: *Science and Information Conference, London, UK*; 2014:372–378.
63. DeLong ER, DeLong DM, Clarke-Pearson DL. Comparing the areas under two or more correlated receiver operating characteristic curves: a nonparametric approach. *Biometrics.* 1988;44(3):837–845.
64. Jr Ambrosio R, AL Caiado, Guerra FP, et al. Novel pachymetric parameters based on corneal tomography for diagnosing keratoconus. *J Refract Surg.* 2011;27(10):753–758.
65. Rabinowitz YS, Rasheed K. KISA% index: a quantitative videokeratography algorithm embodying minimal topographic criteria for diagnosing keratoconus. *J Cataract Refract Surg.* 1999;25(10):1327–1335.
66. Ramos IC, Correa R, Guerra FP, et al. Variability of subjective classifications of corneal topography maps from LASIK candidates. *J Refract Surg.* 2013;29(11):770–775.
67. Rabinowitz YS, Li X, Canedo AL, Ambrosio Jr R, Bykhovskaya Y. Optical coherence tomography combined with videokeratography to differentiate mild keratoconus subtypes. *J Refract Surg.* 2014;30(2):80–87.
68. Benke K, Benke G. Artificial intelligence and big data in public health. *Int J Environ Res Public Health.* 2018;15(12):2796.
69. Luz A, Lopes B, Hallahan KM, et al. Enhanced combined tomography and biomechanics data for distinguishing forme fruste keratoconus. *J Refract Surg.* 2016;32(7):479–494.
70. Kosekahya P, Koc M, Caglayan M, Kiziltoprak H, Tekin K, Atilgan CU. Longitudinal corneal tomographical changes in eyes of patients with unilateral and bilateral non-progressive keratoconus. *Cont Lens Anterior Eye.* 2019;42(4):434–438.
71. Imbornoni LM, Padmanabhan P, Belin MW, Deepa M. Long-term tomographic evaluation of unilateral keratoconus. *Cornea.* 2017;36(11):1316–1324.
72. Ambrósio R, Faria-Correia F, Ramos I, et al. Enhanced screening for ectasia susceptibility among refractive candidates: the role of corneal tomography and biomechanics. *Curr Ophthalmol Rep.* 2013;1(1):28–38.
73. Koh S, Ambrósio Jr R, Maeda N, Nishida K. Evidence of corneal ectasia susceptibility: a new definition of forme fruste keratoconus. *J Cataract Refract Surg.* 2020;46(11):1570–1572.
74. Vinciguerra R, Ambrosio Jr R, Roberts CJ, Azzolini C, Vinciguerra P. Biomechanical characterization of subclinical keratoconus without topographic or tomographic abnormalities. *J Refract Surg.* 2017;33(6):399–407.
75. Krachmer JH, Feder RS, Belin MW. Keratoconus and related noninflammatory corneal thinning disorders. *Surv Ophthalmol.* 1984;28(4):293–322.
76. Belin MW, Ambrósio Jr R. Scheimpflug imaging for keratoconus and ectatic disease. *Indian J Ophthalmol.* 2013;61(8):401.
77. Ambrósio Jr R, Ramos I, Luz A, et al. Dynamic ultra high speed Scheimpflug imaging for assessing corneal biomechanical properties. *Rev Bras Oftalmol.* 2013;72:99–102.
78. Salomão MQ, Hofling-Lima AL, Faria-Correia F, et al. Dynamic corneal deformation response and integrated corneal tomography. *Indian J Ophthalmol.* 2018;66(3):373.
79. Ambrósio Jr R. Percentage thickness increase and absolute difference from thinnest to describe thickness profile. *J Refract Surg.* 2010;26(2):84–86. doi:10.3928/1081597X-20100121-01.
80. Ambrósio Jr R, Alonso RS, Luz A, Velarde LGC. Corneal-thickness spatial profile and corneal-volume distribution: tomographic indices to detect keratoconus. *J Cataract Refract Surg.* 2006;32(11):1851–1859.
81. Belin MW, Khachikian SS. An introduction to understanding elevation-based topography: how elevation data are displayed—a review. *Clin Exp Ophthalmol.* 2009;37(1):14–29.
82. Feng MT, Belin MW, Ambrosio Jr R, et al. International values of corneal elevation in normal subjects by rotating Scheimpflug camera. *J Cataract Refract Surg.* 2011;37(10):1817–1821.
83. Gilani F, Cortese M, Ambrosio Jr RR, et al. Comprehensive anterior segment normal values generated by rotating Scheimpflug tomography. *J Cataract Refract Surg.* 2013;39(11):1707–1712.
84. Roberts CJ, Mahmoud AM, Bons J, et al. A new stiffness parameter in air puff induced corneal deformation analysis. *Investig Ophthalmol Vis Sci.* 2016;57(12).
85. Roberts CJ, Mahmoud AM, Bons JP, et al. Introduction of two novel stiffness parameters and interpretation of air puff–induced biomechanical deformation parameters with a dynamic Scheimpflug analyzer. *J Refract Surg.* 2017;33(4):266–273.
86. Breiman L. Random forests. *Machine Learning.* 2001;45(1):5–32.
87. Salomao MQ, Esposito A, Dupps Jr WJ. Advances in anterior segment imaging and analysis. *Curr Opin Ophthalmol.* 2009;20(4):324–332.
88. Wilson SE, Ambrosio R. Computerized corneal topography and its importance to wavefront technology. *Cornea.* 2001;20(5):441–454.

89. Ambrosio Jr R, Klyce SD, Wilson SE. Corneal topographic and pachymetric screening of keratorefractive patients. *J Refract Surg*. 2003;19(1):24–29.
90. Klein SR, Epstein RJ, Randleman JB, Stulting RD. Corneal ectasia after laser in situ keratomileusis in patients without apparent preoperative risk factors. *Cornea*. 2006;25(4):388–403.
91. Chan CC, Hodge C, Sutton G. External analysis of the Randleman Ectasia Risk Factor Score System: a review of 36 cases of post LASIK ectasia. *Clin Experiment Ophthalmol*. 2010;38(4):335–340.
92. Bohac M, Koncarevic M, Pasalic A, et al. Incidence and clinical characteristics of post LASIK ectasia: a review of over 30,000 LASIK cases. *Semin Ophthalmol*. 2018;33(7-8):869–877.
93. Shetty R, Kumar NR, Khamar P, et al. Bilaterally asymmetric corneal ectasia following SMILE with asymmetrically reduced stromal molecular markers. *J Refract Surg*. 2019;35(1):6–14.
94. Moshirfar M, Tukan AN, Bundogji N, et al. Ectasia after corneal refractive surgery: a systematic review. *Ophthalmol Ther*. 2021;10(4):753–776.
95. Malecaze F, Coullet J, Calvas P, Fournie P, Arne JL, Brodaty C. Corneal ectasia after photorefractive keratectomy for low myopia. *Ophthalmology*. 2006;113(5):742–746.
96. Taneri S, Kiessler S, Rost A, Dick HB. Corneal ectasia after LASIK combined with prophylactic corneal cross-linking. *J Refract Surg*. 2017;33(1):50–52.
97. Maeno S, Koh S, Ambrosio Jr R, Nishida K. Underestimated corneal abnormalities prior to cataract surgery in university hospital settings. *J Cataract Refract Surg*. 2021;47(4):547–548.
98. Vastardis I, Sagri D, Fili S, Wolfelschneider P, Kohlhaas M. Current trends in modern visual intraocular lens enhancement surgery in stable keratoconus: a synopsis of do's, don'ts and pitfalls. *Ophthalmol Ther*. 2019;8(suppl 1):33–47.
99. Wang KM, Jun AS, Ladas JG, Siddiqui AA, Woreta F, Srikumaran D. Accuracy of intraocular lens formulas in eyes with keratoconus. *Am J Ophthalmol*. 2020;212:26–33.
100. Ambrosio Jr R, Belin MW. Imaging of the cornea: topography vs tomography. *J Refract Surg*. 2010;26(11):847–849.
101. Reinstein DZ, Gobbe M, Archer TJ, Silverman RH, Coleman DJ. Epithelial, stromal, and total corneal thickness in keratoconus: three-dimensional display with artemis very-high frequency digital ultrasound. *J Refract Surg*. 2010;26(4):259–271.
102. Salomão MQ, Hofling-Lima AL, Lopes BT, et al. Role of the corneal epithelium measurements in keratorefractive surgery. *Curr Opin Ophthalmol*. 2017;28(4):326–336.
103. Li Y, Chamberlain W, Tan O, Brass R, Weiss JL, Huang D. Subclinical keratoconus detection by pattern analysis of corneal and epithelial thickness maps with optical coherence tomography. *J Cataract Refract Surg*. 2016;42(2):284–295.
104. Pahuja N, Shroff R, Pahanpate P, et al. Application of high resolution OCT to evaluate irregularity of Bowman's layer in asymmetric keratoconus. *J Biophotonics*. 2017;10:701–707.
105. Khamar P, Dalal R, Chandapura R, et al. Corneal tomographic features of postrefractive surgery ectasia. *J Biophotonics*. 2019;12(2):e201800253.
106. Ambrosio Jr R, Nogueira LP, Caldas DL, et al. Evaluation of corneal shape and biomechanics before LASIK. *Int Ophthalmol Clin*. 2011;51(2):11–38.
107. Ambrosio Jr R, Correia FF, Lopes B, et al. Corneal biomechanics in ectatic diseases: refractive surgery implications. *Open Ophthalmol J*. 2017;11:176–193.
108. Eliasy A, Chen KJ, Vinciguerra R, et al. Determination of corneal biomechanical behavior in-vivo for healthy eyes using CorVis ST tonometry: stress-strain index. *Front Bioeng Biotechnol*. 2019;7:105.
109. Chong J, Dupps Jr WJ. Corneal biomechanics: measurement and structural correlations. *Exp Eye Res*. 2021;205:108508.
110. Scarcelli G, Pineda R, Yun SH. Brillouin optical microscopy for corneal biomechanics. *Invest Ophthalmol Vis Sci*. 2012;53:185–190.
111. Scarcelli G, Yun SH. In vivo Brillouin optical microscopy of the human eye. *Opt Express*. 2012;20(8):9197–9202.
112. Shao P, Eltony AM, Seiler TG, et al. Spatially-resolved Brillouin spectroscopy reveals biomechanical abnormalities in mild to advanced keratoconus in vivo. *Sci Rep*. 2019;9(1):7467.
113. Seiler TG, Shao P, Eltony A, Seiler T, Yun SH. Brillouin spectroscopy of normal and keratoconus corneas. *Am J Ophthalmol*. 2019;202:118–125.
114. Kling S, Akca IB, Chang EW, et al. Numerical model of optical coherence tomographic vibrography imaging to estimate corneal biomechanical properties. *J R Soc Interface*. 2014;11(101):20140920.
115. Kling S, Torres-Netto EA, Spiru B, Sekundo W, Hafezi F. Quasi-static optical coherence elastography to characterize human corneal biomechanical properties. *Invest Ophthalmol Vis Sci*. 2020;61(6):29.
116. Spiru B, Torres-Netto EA, Kling S, Lazaridis A, Hafezi F, Sekundo W. Biomechanical properties of human cornea tested by two-dimensional extensiometry ex vivo in fellow eyes: PRK versus SMILE. *J Refract Surg*. 2019;35(8):501–505.
117. Hosoda Y, Miyake M, Meguro A, et al. Keratoconus–susceptibility gene identification by corneal thickness genome-wide association study and artificial intelligence IBM Watson. *Commun Biol*. 2020;3(1):410.
118. Mas Tur V, MacGregor C, Jayaswal R, O'Brart D, Maycock N. A review of keratoconus: Diagnosis, pathophysiology, and genetics. *Surv Ophthalmol*. 2017;62(6):770–783.
119. Rabinowitz YS, Galvis V, Tello A, Rueda D, Garcia JD. Genetics vs chronic corneal mechanical trauma in the etiology of keratoconus. *Exp Eye Res*. 2021;202:108328.
120. Vinciguerra R, Ambrosio Jr R, Elsheikh A, et al. Detection of postlaser vision correction ectasia with a new combined biomechanical index. *J Cataract Refract Surg*. 2021;47(10):1314–1318.
121. Flockerzi E, Hafner L, Xanthopoulou K, et al. Reliability analysis of successive corneal visualization Scheimpflug technology measurements in different keratoconus stages. *Acta Ophthalmol*. 2022;100(1):e83–e90.
122. Flockerzi E, Vinciguerra R, Belin MW, Vinciguerra P, Ambrosio Jr R, Seitz B. Correlation of the Corvis Biomechanical Factor with tomographic parameters in keratoconus. *J Cataract Refract Surg*. 2022;48(2):215–221.
123. Flockerzi E, Vinciguerra R, Belin MW, Vinciguerra P, Ambrosio Jr R, Seitz B. Combined biomechanical and tomographic keratoconus staging: adding a biomechanical param-

eter to the ABCD keratoconus staging system. *Acta Ophthalmol*. 2022;100(5):e1135–e1142.

124. Hashemi H, Heirani M, Ambrósio Jr R, Hafezi F, Naroo SA, Khorrami-Nejad M. The link between keratoconus and posterior segment parameters: an updated, comprehensive review. *Ocular Surf*. 2022;23:116–122.

125. Hashemi H, Asgari S, Panahi P, Mehravaran S, Fotouhi A, Ambrósio R. Corneal ectasia in mothers of Down syndrome children. *Sci Rep*. 2021;11(1):22436.